Local Structure and Electronic State of Atomically Dispersed Pt Supported on Nanosized CeO₂

Matthew Kottwitz,[†,○] Yuanyuan Li,[‡,○] Robert M. Palomino,[§] Zongyuan Liu,[§] Guangjin Wang,[∥,□] Qin Wu,[⊥] Jiahao Huang,[‡] Janis Timoshenko,[‡] Sanjaya D. Senanayake,[§] Mahalingam Balasubramanian,[#] Deyu Lu,[⊥] Ralph G. Nuzzo,[*,†,▽] and Anatoly I. Frenkel[*,‡,§]

†Department of Chemistry, University of Illinois, Urbana, Illinois 61801, United States
‡Department of Materials Science and Chemical Engineering, Stony Brook University, Stony Brook, New York 11794, United States
§Division of Chemistry, Brookhaven National Laboratory, Upton, New York 11973, United States
∥College of Chemistry and Materials Science, Hubei Engineering University, Xiaogan 432000, China
⊥Center for Functional Nanomaterials, Brookhaven National Laboratory, Upton, New York 11973, United States
#Advanced Photon Source, Argonne National Laboratory, Lemont, Illinois 60439, United States
▽Surface and Corrosion Science, School of Engineering Sciences in Chemistry, Biotechnology and Health, KTH Royal Institute of Technology, Drottning Kristinasväg 51, 100 44 Stockholm, Sweden

S Supporting Information

ABSTRACT: Single atom catalysts (SACs) have shown high activity and selectivity in a growing number of chemical reactions. Many efforts aimed at unveiling the structure−property relationships underpinning these activities and developing synthesis methods for obtaining SACs with the desired structures are hindered by the paucity of experimental methods capable of probing the attributes of local structure, electronic properties, and interaction with support—features that comprise key descriptors of their activity. In this work, we describe a combination of experimental and theoretical approaches that include photon and electron spectroscopy, scattering, and imaging methods, linked by density functional theory calculations, for providing detailed and comprehensive information on the atomic structure and electronic properties of SACs. This characterization toolbox is demonstrated here using a model single atom Pt/CeO₂ catalyst prepared via a sol−gel-based synthesis method. Isolated Pt atoms together with extra oxygen atoms passivate the (100) surface of nanosized ceria. A detailed picture of the local structure of Pt nearest environment emerges from this work involving the bonding of isolated Pt²⁺ ions at the hollow sites of perturbed (100) surface planes of the CeO₂ support, as well as a substantial (and heretofore unrecognized) strain within the CeO₂ lattice in the immediate vicinity of the Pt centers. The detailed information on structural attributes provided by our approach is the key for understanding and improving the properties of SACs.

KEYWORDS: single atom, platinum, ceria, multimodal, catalysis, sol−gel
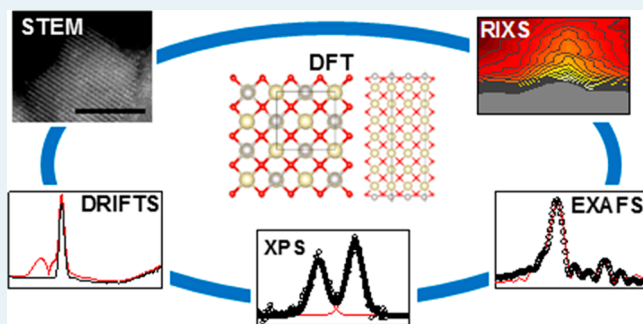
■ INTRODUCTION

Single atoms catalysts (SACs) have been heavily investigated in recent years since the concepts of "single-atom catalysts" and "single-atom catalysis" were first introduced in 2011 by T. Zhang and co-workers.[1] These types of catalysts show high activities and selectivity for many reactions[2−4] and have extremely high atomic efficiency.[5,6] This follows from the fact that ideally in SACs, every atom might contribute to reactivity (in contrast with metal cluster or nanoparticle catalysts, where active sites frequently coexist with nondirectly contributing mass fractions that can change in nature during reaction conditions).[7] Such high atomic efficiency, from the applied point of view, is very important for noble metals, which are naturally scarce yet widely used in industry for a vast number

of important chemical reactions.[8−10] From the fundamental point of view, the distinctive catalytic performances of SACs are correlated with the unique electronic and atomic structure of the single atoms which are distinctly different from those of cluster or nanoparticle catalysts.[11] For instance, many experiments have shown that the active site of the SAC is the positively charged single metal species as present under operando conditions in exemplary catalytic processes (e.g., Pt/MgO for propane combustion, Pt/FeOₓ for CO oxidation, Pd/Al₂O₃ for the selective aerobic oxidation of allylic alcohols,

Au/CeO$_2$ and Pt/CeO$_2$ for water−gas shift reaction, Au/ZrO$_2$ for the selective hydrogenation of 1,3-butadiene to butenes).[1,12−15] Recently, Lu et al. identified the active single-atom complex for CO oxidation over single-atom Ir/MgAl$_2$O$_4$, in which Ir single atoms preferentially bind with CO molecules and the oxidation reaction proceeds through an Eley−Rideal mechanism.[16]

There have been numerous efforts to determine the structure of the active species in SACs. Based on theoretical calculations, some of the important structural features of SACs have been identified (e.g., partially vacant 5d orbital of single Pt atoms/FeO$_x$,[1] Pt^{2+} in a square pocket of O$^{2−}$ ions at a (100) nanofacet of CeO$_2$,[17] PtO$_2$ anchoring with undercoordinated cerium cations at CeO$_2$(111) step edges,[18,19] and Pt anchoring to unsaturated pentacoordinate Al^{3+} centers on the (100) facets of γ-Al$_2$O$_3$[20,21]). Though these structural attributes are believed to play roles in the atomic/electronic structural dynamics that lead to the enhanced activity and stability of SACs,[22] there are other results showing that some SACs are less active or comparable in activity to nanoparticle counterparts for the same catalytic reaction.[23−26] These results imply the existence of other structural attributes that may dominantly control the catalytic properties of SACs, yet currently the understandings of the structure of SACs are quite limited. As a consequence, the relationship between the structure and catalytic properties could not be established. Also, design of new SACs is limited as a result. Due to the high free energy of isolated metal atoms, preventing them from aggregation is vital for SACs, especially under high temperature reductive reaction conditions. Reliance on the strong metal−support interaction and creation of anchor sites in the supports are proposed as effective strategies for stabilizing and trapping single metal atoms under reaction conditions, and they have been applied in many synthesis methods (e.g., wet-impregnation method, modular synthetic approach, derivation from metal−organic complexes, the atomic layer deposition, high temperature atom trapping approach[27]) for preparing stable SACs. However, developing methods to stabilize single atoms on the support is just the first step in catalyst design, for which the ultimate goal should be to develop methods to construct SACs with active structures. Therefore, poor understanding of the structure of SACs is a gap toward rational catalyst design.

But why is it difficult to determine the structure of SACs? The main challenges are (a) the low weight loading of metal, which currently is required by the most strategies for synthesizing SACs and which limits the sensitivity of imaging, scattering, and spectroscopic techniques; and (b) the heterogeneity of the structural motifs of single atom sites (e.g., various speciations as surface sites and dopants within the bulk-like supporting oxide phase). It is acknowledged that samples containing atomically disperse metal species do not necessarily have identical environments around each metal species due to the nonuniform nature of most solid supports.[8,28]

To address the above-mentioned challenges, we chose to focus on developing a characterization approach that provides atomic-level detail of the model SAC systems that feature catalytically relevant structures and electronic properties. To enhance their sensitivity to the SAC properties, we adapted an existing synthesis method of high surface area cerium oxide particles to synthesize isolated Pt atoms with high weight loading, singly dispersed on the oxide support. The characterization tools include scanning transmission electron microscopy (STEM), diffuse reflectance infrared Fourier transform

spectroscopy (DRIFTS), X-ray absorption spectroscopy (XAS), resonant inelastic X-ray scattering (RIXS), and X-ray photoelectron spectroscopy (XPS) that, when combined with density functional theory (DFT), help answer the following key questions: *(1) is it a single atom system? (2) what is the charge state of the isolated metal ions? (3) what is the nature of the nearest environment, including the local perturbations of the support?* The answers to these questions are keys for designing active SACs and understanding working mechanisms.

■ EXPERIMENTAL SECTION

Sample Preparation. To prepare the single atom sample, 0.50 g of cerium(IV) oxide nanopowder (<25 nm) was dispersed in a solution made from 2.0 g of urea and 8 mL of water. Afterward, 0.42 g of cerium(III) nitrate hexahydrate and 3.3 g of a solution (approximately 1 wt % Pt) of chloroplatinic acid hydrate in water were added. All chemicals were purchased from Sigma-Aldrich. Ultrapure water (18.2 MOhm) was provided by a Millipore purification system. The mixture was sealed in a vial and stirred for 24 h in an oil bath at 368 K. The postdeposition sample was separated and washed by 3 cycles of centrifuging/redispersing in water to remove ions from precursors. After drying overnight at 333 K, the sample was crushed into a powder and calcined at 773 K (10 K/min heating ramp). Exclusion of the cerium nitrate hexahydrate precursor and a decrease to 1.9 g of the chloroplatinic acid solution in an otherwise identical procedure was used to prepare the cluster sample. The resulting platinum loading of both samples was measured by ICP elemental analysis (the measured wt % loadings of the single atom and surface loaded samples used in this work were 1.84% and 1.74%, respectively).

Scanning Transmission Electron Microscopy Characterization. Aberration corrected high-angle annular dark-field−scanning transmission electron microscopy (HAADF-STEM) was used to image the samples. The samples were dispersed in water and drop-casted onto lacey carbon copper grids (Ted Pella) for analysis using either a JEOL 2200FS operated at 200 kV (100 pm resolution limit) or an FEI Themis Z operated at 300 kV (60 pm resolution limit).

Diffuse Reflectance Infrared Fourier-Transform Spectroscopy. The spectra were collected using a Nicolet 6700 FTIR spectrometer equipped with a rapid-scanning liquid-nitrogen-cooled mercury cadmium telluride (MCT) detector and a Praying Mantis High Temperature Reaction Chamber (Harrick Scientific Products). Prior to each measurement, the sample was heated at 10 °C/min to 300 °C under He and held for 10 min. The sample was subsequently cooled to room temperature, and the background spectrum (256 scans) was collected with a resolution of 4 cm$^{−1}$. A 10% CO/He mixture was then flowed through the chamber for 1 h before the spectra featuring CO adsorption were acquired. Afterward, the chamber was purged with He for 1 h before the CO desorption spectra was acquired.

X-ray Photoelectron Spectroscopy. A commercial SPECS AP-XPS chamber equipped with a PHOIBOS 150 EP MCD-9 analyzer at the Chemistry Division of Brookhaven National Laboratory (BNL) was used for XPS analysis. The Ce 3d photoemission line with the strongest Ce^{4+} feature (916.9 eV) was used for the energy calibration. The powder sample (Pt-CeO$_2$ catalyst) was pressed on an aluminum plate and then loaded into the AP-XPS chamber. Ten mTorr of H$_2$ or 10 mTorr of CO + 23 mTorr of H$_2$O was leaked into the reaction

chamber through a high precision leak valve. O 1s, Ce 4d, Pt 4f, and Pt valence band XPS regions were collected at 300 K under the reaction gas environment.

X-ray Absorption Spectroscopy and Resonant Inelastic X-ray Scattering. X-ray absorption spectroscopy (XAS) and resonant inelastic X-ray scattering (RIXS) were performed at Beamline 20-ID-C of the Advanced Photon Source (APS), Argonne National Laboratory. The sample powders were loaded in a quartz tubing (2 mm I.D., 2.4 mm O.D.) and mounted in a Clausen cell.[29] The incident beam was monochromatized with a Si(111) monochromator and focused using a toroidal mirror. Harmonic rejection was also provided by the toroidal mirror. A pair of slits were used to define the beam to a size of 300 μm horizontally and 200 μm vertically. The energy scale was calibrated by defining the first derivative maximum of Pt foil as 11564.00 eV. The XAS data were collected in fluorescence mode by using a Vortex (Hitachi) silicon drift detector.

The emission spectra were obtained using a 100 mm diameter spherical, strip-bent crystal analyzer of 0.5 m bending radius. The analyzer was acquired from XRS Tech LLC, New Jersey. The (933) reflection was used to measure the valence band emission. The scattering angle was at 90 deg to minimize the intensity of the elastic peak. The scattered radiation was detected using a Dectris Pilatus 100 K area detector. A region of interest that encloses the area encountered by the scattered radiation was carefully chosen to minimize background scattering and maximize the signal-to-noise. The instrumental energy resolution was determined to ~2.7 eV by monitoring the fwhm of the elastic scattering line from a thin Kapton sheet.

Computational. All the calculations were performed with density functional theory (DFT) using the projector augmented wave (PAW) method[30,31] as implemented in the Vienna ab initio simulation package (VASP)[32] with a plane-wave energy cutoff of 500 eV. The generalized gradient approximation (GGA) of DFT in the form of the Perdew–Burke–Ernzerhof (PBE) exchange-correlation functional[33] was used. Ce semicore states (5s, 5p, and 5d) were treated explicitly as valence electrons in the pseudopotential, and the Ce 4f electrons were treated with the DFT+U method[34] with an effective Hubbard U of 5.0 eV.[35,36] The optimized lattice constant of bulk CeO_2 is 5.50 Å, which is about 1.6% longer than 5.41 Å measured in the experiment.[37] A similar trend of overestimation of lattice constant using PBE+U is known in the literature.[38] The Pt-passivated CeO_2 (100) slab was modeled with seven Ce layers and eight oxygen layers without surface reconstruction, and the central O–Ce–O trilayer fixed at the bulk geometry during structure optimization. A vacuum layer of 15 Å along the z direction was used in the slab model to prevent spurious interactions of image cells. The Brillouin zone of this slab model was sampled with a 6 × 6 × 1 Γ-centered k-point grid. At the end of the structure optimization, forces on each atom were less than 0.01 eV Å^{-1}. Fully optimized atomic models were obtained from DFT, including Pt on a cuboctahedral $Ce_{40}O_{80}$ nanoparticle and several CeO_2 (100) slab models. Structural parameters from these models, such as Pt–O and Pt–Ce distances and Pt coordination numbers, were used to corroborate results from the EXAFS measurement. The charge state of Pt was determined from Bader charge analysis[39] in order to corroborate the XPS measurement.

RESULTS AND DISCUSSION

In this section, we first introduce a new method which, based on the data presented, yields materials carrying high concentrations of single-Pt-atom sites that are localized at the ambient (gas-phase-contacting) surfaces of the nanoscale ceria support. The very low mass fraction of other bonded forms of Pt, whether present as bulk dopants or surface-bound clusters (Pt-metal or PtO_2, vide infra) makes it possible to extract more meaningful conclusions from multimodal methods of structural characterization that are complicated by ensemble averaging when applied to a heterogeneously speciated system.[40]

The synthetic method that we developed for preparing Pt/CeO_2 SAC is shown schematically in Figure 1. It was exploited
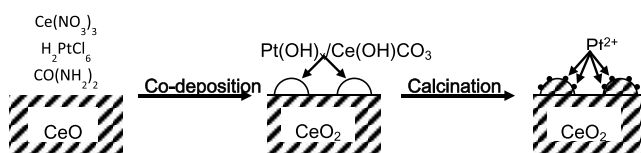
Figure 1. Preparation schematic of single atom Pt on CeO_2. Exclusion of the $Ce(NO_3)_3$ precursor results in PtO_x clusters on CeO_2 while exclusion of H_2PtCl_6 results in CeO_2 on CeO_2.

to generate (*vide infra*) the materials comprised of nearly homogeneous dispersions of the single-surface Pt atoms on CeO_2—a hydrothermal sol–gel process that deposits Pt-doped Ce(OH)CO$_3$ nanoparticles as a precursor on the surface of a commercial CeO_2 support material.[41,42] Subsequent calcination leads to a structural transformation of the precursor phase to supported CeO_2 nanoparticles bearing isolated Pt atoms on their surface. The sol-based "impregnation" process serves to effectively increase the numbers of Pt atoms present at the surface of the support. Although not a subject considered in depth in the current report, this method can be used to generate hybrid Pt/CeO_2 SACs supported on other oxide support materials—SiO_2 and Al_2O_3 as notable exemplars—with appropriate modifications made to the reported synthetic methods. Compared to incipient wetness impregnation[42−45] and solution combustion,[46−48] synthetic approaches that have been reported for the preparation of ceria-supported Pt-SACs, the newly developed synthetic method improves the weight loading of metal atoms on the surface of the support. In the case of incipient wetness impregnation, metal weight loadings below 0.5% are generally required to avoid aggregation of Pt-precursor species into clusters.[45,49] Subsequent etch-back processes also have been described that make it possible to remove Pt atoms that are present in cluster-like speciations, but the impact of these procedures on the chemistry of active supports such as ceria has not been fully established.[13] Solution combustion synthesis, on the other hand, is less efficient in generating surface localizations of the Pt, producing instead significant populations of bulk/substitutional habits of Pt atoms with complex/heterogeneously speciated metal atom-support coordination environments.

In the section that follows we describe the structure of the as-prepared Pt/CeO_2 catalyst, documenting features of the conversion of precursor phases that mediate its formation. The correlated data from multimodal techniques address questions that include: (1) *the nature of the homogeneous speciation of the single atoms catalysts obtained via a new preparative method* (investigations combining STEM, CO-chemisorption exam-

ined via DRIFTS, XPS and XAS); (2) *the valence state of singly disposed Pt atoms present on the ceria surface* (investigations of CO-chemisorption combining DRIFTS and XPS); (3) *the nature of the complex interactions that occur between single Pt atom sites and the ceria support, the substantial near-surface structural modifications they elicit, and their effect on the electronic properties of the Pt atom sites* (correlated data combining XPS, RIXS, and XAS measurements); and (4) *the unexpected geometry that defines the bonding of single Pt atoms to the ceria support* (insights from the correlations of XPS and XAS data with DFT calculations).

The structure of the synthesized materials obtained following the final calcination step at 773 K was examined by STEM (Figure 2). The crystalline structure of the ceria
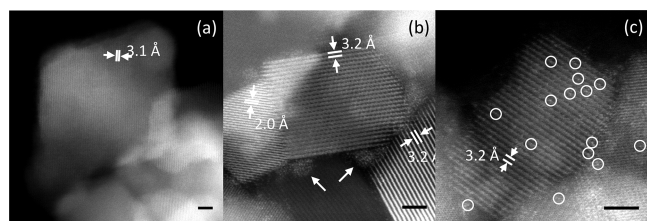
Figure 2. Scanning transmission electron micrographs of (a) unmodified ceria support, (b) PtO_x clusters on ceria support as produced via a traditional incipient wetness method and (c) isolated Pt atoms on the surface of deposited CeO_2 as produced via the CeO_2 sol-impregnation method detailed in Figure 1. Scale bars are 2 nm. Additional images of the PtO_x cluster and single atom samples can be found in Figure S1. STEM images of a sample prepared via the sol–gel-based synthesis with the Pt precursor excluded can be found in Figure S2.

support is clearly revealed by the representative STEM data shown in Figure 2a. The deposition of Pt on this material by a conventional incipient wetness method (see Experimental Section) yields, after calcination, large (1.5–2 nm) PtO_x clusters on the surface of the commercial CeO_2 (Figure 2b), a result consistent with previously reported in literature. The ceria sol-impregnation method of Figure 1 yields a very different material post calcination. In this case the STEM data reveal (via Z-contrast) the presence of isolated Pt atoms concentrated on the surface of regions of sol-derived CeO_2 (Figure 2c). The data presented here (and that which follow) demonstrate that the sol-process makes it possible to obtain isolated Pt surface atoms at high effective mass coverages. We note that interpretations of the STEM data (that presented in the figure and others as shown in Figure S1) remain somewhat qualitative due to the poor Z-contrast of Pt against a more intense Ce-dominated background. This is most evident in determining the positions of the isolated Pt atoms relative to the surface of a CeO_2 substrate when viewing regions precisely aligned along a zone axis (these materials are also highly sensitive to radiation damage due to the mobility of the Pt surface atoms seen under the 300 keV beam). As we show below, XAS data allow a more quantitative determination of the surface speciation and coordination environments of the Pt single atoms which, when complemented with computational modeling, provides locations and structural trends for the atoms on the surface of the CeO_2 support. Even so, while a thorough STEM examination of the materials has not resulted in observation of Pt-based clusters or nanoparticles, an independent verification of the absence of such speciations remains an important requirement. To address this concern, we performed CO-chemisorption studies monitored by DRIFTS—a technique that detects all Pt surface atoms
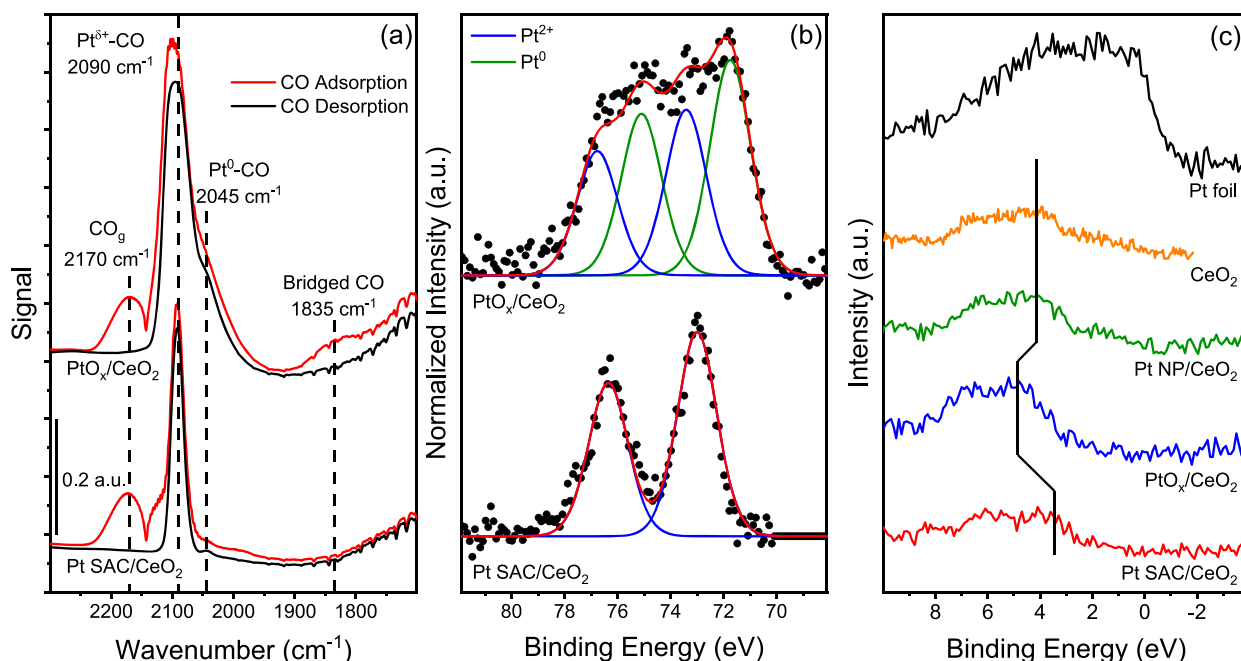
Figure 3. (a) DRIFTS spectra after CO adsorption (red) and CO desorption (black) of PtO_x clusters on CeO_2 (incipient wetness sample) and Pt single atoms on CeO_2 (sol-impregnation sample). Characteristic peaks for CO in the gas-phase (2170 cm^{-1}), adsorbed atop $Pt^{\delta+}$ or Pt^0 (2090 and 2045 cm^{-1}, respectively), and bound to a bridge site (1835 cm^{-1}) are noted. (b) The Pt 4f region of XPS spectra for the PtO_x cluster and Pt single atom samples with Pt^{2+} (blue) and Pt^0 (green) fitting curves. (c) Valence band XPS spectra of the afforementioned samples with the addition of Pt foil, commercial CeO_2, and H_2 treated (20 mTorr H_2 at 623 K for 30 min) PtO_x on CeO_2 (noted Pt NP/CeO_2) samples for comparison.

present—to confirm the uniform single atom speciation and, in conjunction with XPS data, determine their oxidation state(s). These data are presented in the section that follows.

DRIFTS data for two forms of Pt supported on ceria are shown in Figure 3—the first for a standard sample of the larger (1.5−2 nm) PtO_x clusters (Figure 2b) afforded by an incipient wetness preparation method and the second for the sol-derived SACs. As shown in Figure 3(a), characteristic peaks appear between 1700 and 2300 cm^{-1} corresponding to the vibrational/stretching modes of CO adsorbed on Pt sites. The peak at 2170 cm^{-1} is due to gas-phase molecules, and it disappeared after the CO is flushed away. The peaks at about 2090 and 2045 cm^{-1} are assigned to the modes of CO molecules adsorbed atop a Pt atom.[50,51] The peak at about 1835 cm^{-1} is assigned to CO molecules bound to a bridge site.[52] Binding at the latter site is only seen for the PtO_x cluster sample. This species is also very weakly bound, being lost when the CO overpressure is removed (the atop-site bonding persists, suggesting higher binding energy for this moiety).[53] It is also noteworthy that the highly asymmetric line shape for the atop species on PtO_x strongly supports bonding interactions occurring at heterogeneously speciated Pt sites, a point we discuss in more detail below. These data demonstrate a heterogeneity that likely convolves distinctions of both composition and valence state within these clusters (vide supra). For the Pt SACs, a single narrow yet intense mode is seen, one assignable to CO bound atop single metal sites. The frequency of this mode, appearing at 2090 cm^{-1}, is consistent with bonding interactions of CO on a higher valence ($Pt^{\delta+}$) site. The additional mode seen for the PtO_x clusters, a peak centered at ∼2045 cm^{-1}, corresponds to an atop bonded CO molecule on Pt^0.[45] While the CO probe gas may partially reduce the PtO_x clusters, examination of the XPS measurement of the as-prepared sample demonstrates an initial population of Pt^0 atoms. The Pt SAC sample displays a very weak feature centered at ∼2045 cm^{-1}, but this may be attributed to noise due to the lack of such a feature in the CO adsorption curve and the lack of evidence for a Pt^0 speciation in the XPS data. The data therefore strongly support the presence of a significant density of single higher valence $Pt^{\delta+}$ surface atoms in the SAC material, which contrasts markedly with the heterogeneous, mixed valence $Pt^{\delta+}/Pt^0$ speciation seen for the PtO_x clusters. The assignments for the formal oxidation states of the Pt present in each case follow more conclusively from the data of XPS studies.

Exemplary XPS data for the materials examined above are shown in Figure 3(b). Again, for purposes of comparison, Pt 4f XPS core level data for both ceria supported SAC and PtO_x materials are presented in the figure. For the PtO_x cluster sample, the spectrum is well fit by two groups of peaks (one group in blue and one group in green). The binding energies of these components support an assignment of the Pt oxidation state in the one case (green) to Pt^0, and the other (blue) to Pt^{2+}. For Pt^0, the experimentally observed binding energy of the Pt-$4f_{7/2}$ core level is 71.5 and 73.1 eV for the Pt^{2+} species. These values are slightly higher than those reported for reference compounds with these oxidation states, a shift that is likely a result of the final state effects from bonding perturbations due to the CeO_2 support and/or the small size of the PtO_x clusters.[54,55] For the SACs, it is most significant that no contributions assignable to Pt^0 are evidenced, confirming the homogeneity of Pt^{2+} sites in the single atom sample in contrast to the mixed Pt^{2+}/Pt^0 speciation of the

materials obtained via standard solution-based impregnation methods.

The valence band spectrum of Pt SACs on CeO_2 was measured to examine the valence electronic structure of near surface Pt and Ce atoms. As references, the spectra of a Pt foil, CeO_2, as-prepared PtO_x/CeO_2, and Pt NPs/CeO_2 reduced in H_2 were also collected (Figure 3c). For Pt foil, the valence electronic structure is dominated by a broad partially occupied 5d-band in the region of −1.0 to 8.0 eV.[56,57] For CeO_2, the valence band structure is dominant in the range of 2.0 to 8.0 eV, and the broad feature seen here is due to hybridized O 2p states.[58−60] The valence band spectra of all the various Pt/CeO_2 samples are similar to that of CeO_2, which is expected because of its dominant mass fraction in all of the latter samples. In Figure 3(c), the vertical line shows the positions of the maxima of XPS spectra for CeO_2 standard and various samples. For the as-prepared SAC sample, the maximum shifts toward lower binding energy while for the as-prepared PtO_x sample it shifts toward higher binding energy. After the clusters in the latter sample are reduced, the maximum shifts back and is very close to that of the CeO_2 standard. In addition, a weak peak appears after reduction at about 1.6 eV. This peak is due to the splitting of Ce 4f states and can be assigned to the occupied (Ce^{3+}) Ce 4f state.[60−63] For the as-prepared samples, the shifts relative to CeO_2 standard illustrate the different strong support interactions that occur between Pt and ceria, ones causing the marked electronic structure changes for both CeO_2 and Pt atom sites.

To more completely examine the electronic structure of the Pt SACs, we performed RIXS measurements. Figure 4 shows the RIXS planes of the Pt SAC materials on CeO_2, metallic Pt nanoparticles supported on carbon as taken from previous work,[64] along with the data for PtO_2 and Pt foil standards. The horizontal axis is the incident energy, scanned across the Pt L_3 edge energy (11564 eV). The vertical axis is the energy transfer representing the energy difference between the incident and emitted photon energies. The RIXS process can be viewed schematically as one including three states and two steps.[65,66] In Step 1, starting from the initial state, the incident photon excites a core level Pt 2p electron to unoccupied Pt 5d valence states, which leads to the creation of an intermediate state with a core hole left at the core level. In the following step, from the intermediate state, an electron from the occupied region of the Pt 5d valence state fills the core hole, producing the photon emission that yields the final state configuration. The RIXS planes therefore provide information related to both the unoccupied and occupied regions of the Pt 5d states. The energy transfer, here, arises from valence excitations. In the current RIXS data (Figure 4), the main features observed are due to the transitions occurring between occupied and unoccupied Pt 5d (dd) states. In RIXS planes, the zero-energy transfer point corresponds to the position of the elastic peak, which serves for energy calibration purpose and indicates the state in which no energy is deposited into the sample. For a Pt foil, the elastic peak and the valence-band excitations merge together (Figure 4a), as expected for a case where the Fermi level lies within a partially filled band. For PtO_2, a material with a bandgap in the range of 1.3−1.8 eV, a gap is seen between the elastic peak (zero energy transfer) and the lowest unoccupied 5d electronic states, one corresponding to a gap between the unoccupied 5d and occupied 5d states, with the Fermi level lying in the gap. The merging of the elastic peak and the valence-band excitations has been reported to occur in
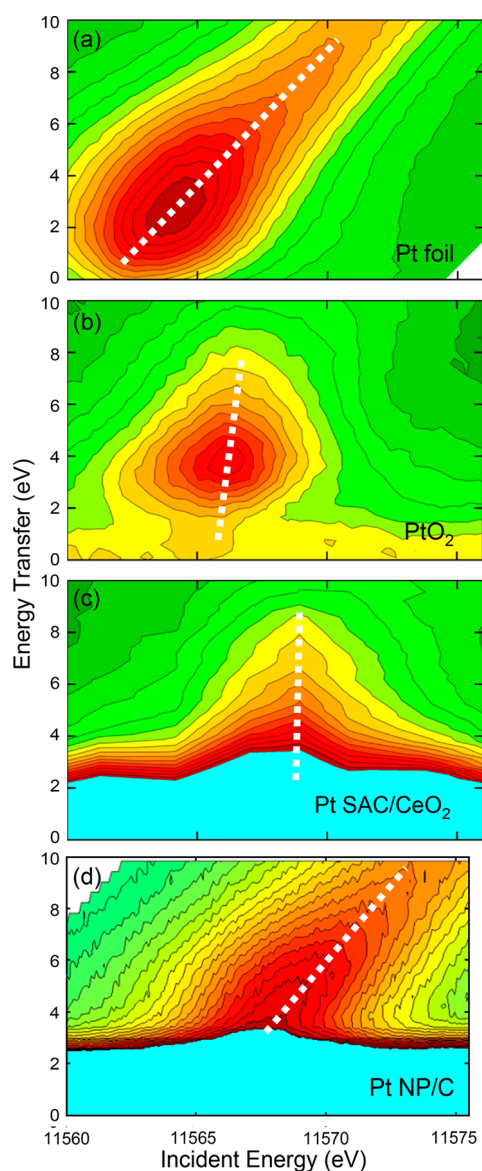
Figure 4. RIXS planes measured across Pt L₃ edge for (a) Pt foil and (b) PtO₂ standards, (c) Pt single atoms on CeO₂ and (d) Pt NPs on carbon from a previous work. Reproduced with permission from ref 64. Copyright 2014 Wiley-VCH.

a simulated Pt_{37} cluster,[64] a simulated Pt_6 cluster, and a 2 wt % Pt/Al_2O_3 sample with a particle size about 1 nm.[67] The latter observations affirm the metallic electronic structure of the small Pt clusters in these cases. For both the Pt single atom sample and nanoparticles samples, as shown in Figure 4(c) and (d), the d band features lower than the 2 eV in energy transfer could not be observed due to the strong background from the elastic peak. Despite that, a notable difference is observed in the shape of the RIXS signal for the Pt SAC material on ceria as compared to that for a C-supported sample of metallic Pt NPs. We see here that for both the Pt foil and Pt nanoparticle sample, the contribution of d band tails along the diagonal of the RIXS plane (shown by white line in Figure 4(a) and (d)), which corresponds to a scan of the incident energy at the fixed emission energy. Such emission energy is associated with the transition between the occupied Pt 5d to Pt 2p levels. For PtO₂ and Pt single atoms sample, similar features are not observed; instead, the contribution of d band tails along the vertical axis

due to the Pt 5d-O 2p transitions that occur at higher energy transfer, suggesting the localized character of the Pt 5d states.[68] The similarity between the RIXS behavior in PtO₂ and Pt SAC sample validates this hypothesis because in both samples Pt is bonded to the O atoms (XAS data described below provide an independent support of this conclusion as well).

XANES spectra in Figure 5a further document the strong interaction occurring between Pt and O in the ceria-supported
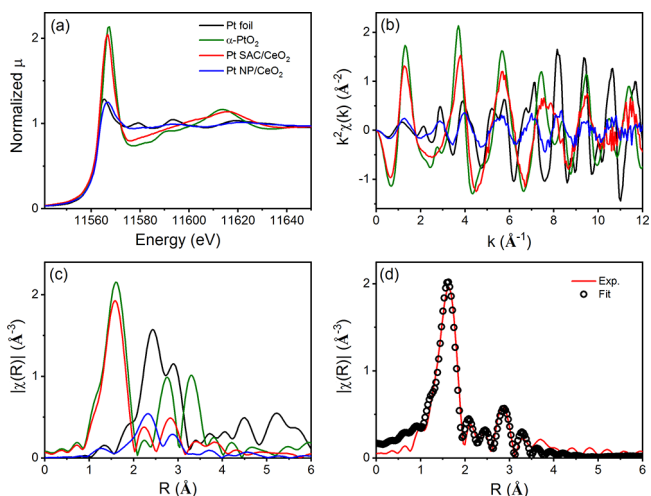
Figure 5. Pt L₃ edge XAS spectra of Pt single atoms on ceria support. For comparison, the XAS spectra of standards (Pt foil and α-PtO₂) and ceria supported Pt nanoparticles (after reduction in H₂ of the PtOx cluster on CeO₂ sample; reduction condition: 3.5% H₂ (balance He) at 423 K for 1 h; data were collected at room temperature after the treatment) are included. (a) XANES, (b) EXAFS spectra in k space, (c) EXAFS spectra in R space, and (d) comparison of experimental spectrum with the fit for the single atom sample. In Figure 5c, the k range used for Fourier transform is 2.0 to 11.0 Å⁻¹ for all spectra in the main figure. In Figure 5d, for the fitting, the k range is 2.0 to 13.0 Å⁻¹ and the R range is 1.0 to 3.5 Å.

single atom sample. For the SAC, the white line at about 11567 eV is quite high and closely resembles that of PtO₂. A reference material for this part of the study was generated by in situ reduction of the PtOₓ nanoparticles (the material present in Figure 2b) in a H₂ atmosphere (as described in the Experimental Section). The intensity of the white line seen in this case is similar to that of Pt foil, suggesting the metallic nature of the nanoparticles present in the reduced sample. Though the white line of single atoms sample is similar to that of PtO₂, the XANES spectrum of the single atoms sample shows distinct features in the energy range of 11570 to 11630 eV. Important differences between the spectra of the SAC and PtO₂ samples are also observed in the EXAFS region, ones that include: (1) in k-space spectra (Figure 5b), in addition to the lower oscillation amplitude, the spectrum of the single atoms sample shows different shapes in the range of 6 to 9 Å⁻¹; and (2) in R-space (Figure 5c), though each of the spectra for PtO₂ and SAC samples have a pronounced peak at about 1.5 Å which is assigned to the Pt−O contribution, the PtO₂ data contains two additional pronounced peaks in the range of 2.5 to 4.0 Å, while in the same region, the SAC data show a contrasting relatively strong peak at about 2.8 Å and weak features in the range of 3−4 Å. For PtO₂, the additional two peaks in the range of 2.5 to 4.0 Å are contributed by the second coordination shell (Pt−Pt) and Pt−O−Pt−O−Pt linear

multiple scattering paths. The spectrum of Pt foil in comparison shows two peaks in the region of 2.0 to 3.5 Å, ones due to the contribution of the first nearest Pt−Pt scattering path. The XAS spectrum of the reduced Pt nanoparticles on ceria has similar spectral shape to that of Pt foil, but with a lower intensity of the peaks, in agreement with the metallic and nanosized nature of the former sample. For the SAC sample, the R-space EXAFS spectrum shows two peaks in the region of 2.0 to 3.0 Å, with the intensity of the shorter R-space distance peak being lower than the one at larger R values. In the XAS data for a Pt foil, however, an opposing trend is seen. According to the above raw data examination, we could conclude that the XAS spectra of the single atoms sample show unique features in the region of 2.0 to 3.5 Å. Such uniqueness could also be observed by comparing wavelet transform (WT)-EXAFS (Figure S3) of the as-prepared Pt single atoms/ceria with reduced Pt cluster/ceria, Pt foil, and PtO_2. Those features could not be explained by the contributions of Pt−Pt in metal or oxide, suggesting that a new Pt-X (most likely Pt−Ce) contribution should be considered (more details about the tested models and best fitting results are presented in the following section).

EXAFS data fitting was performed to quantify the nature of the local structural features present around Pt in the ceria supported SACs. The XAS data were processed and analyzed using the Ifeffit package.[69] The amplitude reduction factor S_0^2 was determined by fitting the spectrum of Pt foil, which was measured at the same beamline. This value of S_0^2 (0.83) was then used in fitting the spectrum of the SAC sample. To fit the latter data, two possible models were considered and tested. Model 1 included Pt−O, Pt−Pt, and Pt−O paths, while Model 2 included Pt−O, Pt−Ce, and Pt−O paths. Only Model 2 provided reasonable results and good agreement between the experimental and fitted spectra, as shown in Figure 5d. The structural parameters for Pt−Pt, obtained by using Model 1, are not physically reasonable, and the fit quality is much worse than for Model 2. The best fitting results are summarized in Table 1. The absence of detectable (beyond the sensitivity of

Table 1. Summary of the Best Fit Results as Displayed in the Figure 5d

Bond	N	R (Å)	σ^2 (Å²)
Pt−O	4.2 ± 0.1	1.995 ± 0.002	0.0011 ± 0.0005
Pt−Ce	4 ± 1	3.34 ± 0.01	0.006 ± 0.001
Pt−O	5 ± 1	3.57 ± 0.01	0.004 ± 0.005

EXAFS) Pt−Pt contributions confirms that in the SAC sample, Pt atoms are predominantly singly dispersed, in agreement with the STEM and DRIFTs results discussed above. The fitting results further suggest that the Pt in the SAC interacts strongly with the support as evidenced by the significant contributions from Pt−O and Pt−Ce scattering paths.

Based on the EXAFS measurements of the as-prepared SAC sample, on average there are four oxygen atoms that form the nearest-neighbor shell of Pt with a Pt−O bond length of 1.995 Å and four to five Ce atoms in the second nearest-neighbor shell of Pt with a Pt−Ce distance of 3.34 Å. These coordination numbers and distances pose strong geometric constraints to the local atomic arrangement around the Pt atom and allow us to rule out scenarios of a Pt atom embedded in the ceria matrix or adsorbed on the clean ceria (111) surface. The most notable reason here is that the Pt−O and

Pt−Ce distances are far shorter than the corresponding Ce−O and Ce−Ce distances (2.34 and 3.83 Å, respectively[70]), suggesting that a substantial local strain is generated in the nearest vicinity of Pt atoms, of a magnitude suggesting a broader need to define precise placement sites of the Pt on ceria support in ways that correspond to the observed Pt−O and Pt−Ce coordination numbers and distances. To address this need, we performed theoretical DFT simulations, the results of which are discussed below.

In order to search for a possible location of Pt, eight candidate structures were examined, whose structure models are shown in Figures 6, S4, and S5. We started from a previously reported structure, where a single Pt atom is placed on one of the (100) nanofacets of a cuboctahedral $Ce_{40}O_{80}$ nanoparticle (NP) in a truncated octahedral shape with O-terminated (111) and very small (100) nanofacets.[17,71−73] Although the (100) surface is much less stable than the (111) surface of ceria,[74] the (100) nanofacets are in fact abundant in ceria nanostructures.[72,73] In this $PtCe_{40}O_{80}$ NP model, the Pt atom is surrounded by four O atoms in a square shape with the Pt−O bond length of 2.05 Å,[75] in reasonable agreement with the EXAFS results. There are four Ce atoms in the second shell;[75] however, the Pt−Ce distance has not been reported. As we will show below, the Pt−Ce distance is the key result that favors our ceria (100) surface model over the reported $PtCe_{40}O_{80}$ NP model.

We performed the structure optimization of the $PtCe_{40}O_{80}$ NP model (see Figure S4 g) and found that the average Pt−O bond length is 2.04 Å, in close agreement with previous calculations.[75] The Pt−Ce distance found in this optimized structure, however, turns out to be 3.05 Å, a distance that is almost 9% shorter than the value of 3.34 Å value determined from the EXAFS data. To further investigate whether the local structural motifs of the ceria support contribute to this discrepancy, we constructed six slab models containing isolated Pt atoms on a small ceria cluster, mimicking the (100) nanofacets, on the ceria (111) surface (Figure S4 and S5). We found that both the average Pt−O bond length (2.03 Å) and Pt−Ce distance (3.07−3.08 Å) are similar to those in the $PtCe_{40}O_{80}$ NP model (see Table S1).
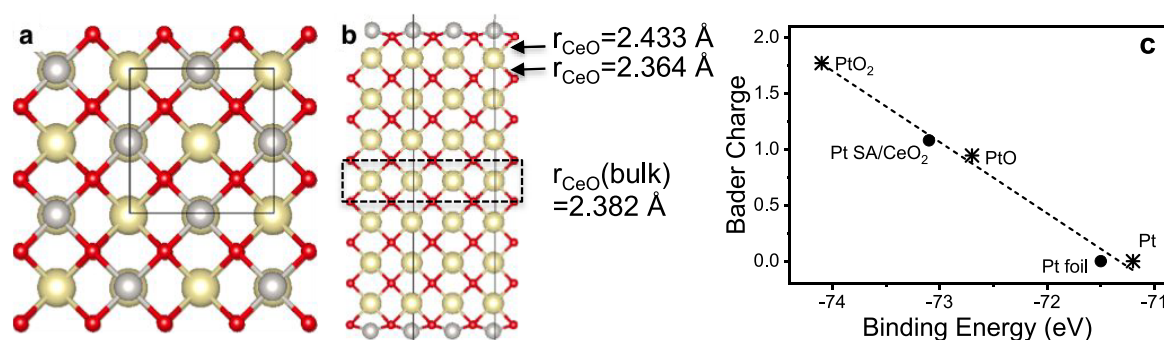
The underestimation of the Pt−Ce distance in these models can be attributed to the undercoordination of Ce atoms. For example, in the $PtCe_{40}O_{80}$ NP model, Ce atoms in the second shell of the Pt atoms are located at the edge of the (111) and (100) nanofacets, with a coordination number of 6 as compared to 8 in the bulk ceria. As a consequence, the average Ce−O bond length between the first shell O and the second shell Ce in the $PtCe_{40}O_{80}$ NP (2.343 Å) is 0.039 Å shorter than that calculated in the bulk (2.382 Å). It is very likely that local structural motifs with less undercoordinated Ce atoms in the second shell may have a longer Ce−O bond length and hence a longer Pt−Ce distance. To verify this hypothesis, we constructed a model of a ceria (100) surface fully passivated by Pt atoms as shown in Figure 6. The structure is kept symmetric in the surface normal direction with Pt atoms occupying the hollow sites. Separate calculations show that Pt atoms at the on-top sites are unstable. The unit cell, as shown in Figure 6a and b, has stoichiometric CeO_2 plus 4 Pt atoms (two on each side) and 4 extra O atoms (Pt_4/O_4/CeO_2 (100)). Like the bulk, all the second shell Ce atoms in this model have a coordination number of 8. This structure is stable against separation into CeO_2, Pt, and PtO_2 by 0.28 eV per Pt atom (see details of the reaction energies in Table S2).

Figure 6. Top (a) and side (b) views of the Pt-passivated ceria (100) surface (The 3D structure of this model is shown in Figure S6). The structure consists of Pt atoms occupying the hollow sites with 4 additional O atoms surrounding. Black lines indicate the unit cell. Pt: gray; Ce: light gold; O: red. The dashed box in (b) indicates the central O−Ce−O trilayer fixed at the bulk geometry. (c) Linear dependence of theoretical Bader charge on the Pt $4f_{7/2}$ core level binding energy for Pt, PtO, PtO_2 (asterisk markers), Pt single atoms on CeO_2 and Pt foil (dot markers). Dashed line is the linear fit.

As a result, both the Pt−O bond length (1.987 Å) and Pt−Ce distance (3.32 Å) are in excellent agreement (within 0.5% relative error) with EXAFS measurements. Besides confirming the experimental (XAS) results, theory plays an additional role here. Our calculations revealed that the average Ce−O bond length between the top layer O and the second layer Ce increases to 2.433 Å, a significant local strain, given that the corresponding bond length in the bulk is 2.382 Å. The average Ce−O bond length between the second layer Ce and the third layer O is 2.364 Å, slightly shorter than the bulk value.

We further analyzed the charge state of Pt in this model using the Bader charge analysis.[39] The resulting Bader charge is 1.079, which is close to the value of 0.944 in PtO but far away from the value of 1.770 in PtO_2. Bader charge analysis indicates that the charge state of Pt in the ceria (100) model is close to +2. In Figure 6, we plot the Bader charge from theory against the Pt $4f_{7/2}$ core level binding energy of Pt foil, PtO, PtO_2, and the SAC sample before the chemical reaction. First we see that there is a very clear linear relationship indicated by the dashed line between the Bader charge of Pt and the Pt $4f_{7/2}$ binding energy. If we assume the Pt-passivated ceria (100) model has the same binding energy as the SAC sample, then this data point falls on the dashed line, indicating that the Pt-passivated ceria (100) model yields the correct charge state of Pt in the SAC sample. In addition to that, in the Pt-passivated ceria (100) model, the Pt density is 6.6 atoms/nm², i.e., close to that estimated for the SAC sample (SI), which, again, validates the $Pt_4/O_4/CeO_2$ (100) structure (Figure 6).

CONCLUSIONS

In summary, we show the capability of determining the atomic and electronic structure of SACs by employing a new multimodal approach which involves complementary experimental techniques (STEM, DRIFTS, XPS, RIXS, and XAS) and DFT calculations on a model catalyst with single Pt atoms (1.8% of weight loading) localized on the surface of ceria support. This characterization approach provides detailed information on SACs: the position and geometry of single atoms on the support, the bonding of the single atom with the support, the effects of single atoms on the electronic structure of the support, the strain in the lattice due to the accommodation of single atoms, and the charge state of the single atom. With the comprehensive information on structural attributes of SACs provided by this approach, connections

between synthesis and catalytic properties could be made. For example, in studying the model catalyst of Pt/CeO_2, the Pt single atom interacts with support by forming the Pt−O−Ce bonds which in some works is believed to be a consequence of the strong metal−support interaction and therefore the reason for the high stability of single atoms. However, in our ongoing work which studies the stability of Pt/CeO_2 in reduction conditions (CO or H_2) at elevated temperatures, we find that both the bonding between the metal atoms with the support and the distance between isolated Pt atoms should be considered in improving the thermal stability of SACs. Another important outcome of this work is that it highlights the prospect of possible synergies that might exist between the activity of SACs and strained surface states of their oxide support.

◼ ASSOCIATED CONTENT

Ⓢ Supporting Information

The Supporting Information is available free of charge on the ACS Publications website at DOI: 10.1021/acscatal.9b02083.

> Additional STEM images, WT-EXAFS, input models for DFT calculations, details on the results of DFT calculations, and estimation on the Pt density for the SAC sample (PDF)

◼ AUTHOR INFORMATION

Corresponding Authors
*E-mail: r-nuzzo@illinois.edu.
*E-mail: anatoly.frenkel@stonybrook.edu.

ORCID Ⓘ
Robert M. Palomino: 0000-0003-4476-3512
Zongyuan Liu: 0000-0001-8526-5590
Qin Wu: 0000-0001-6350-6672
Sanjaya D. Senanayake: 0000-0003-3991-4232
Anatoly I. Frenkel: 0000-0002-5451-1207

Present Address
▢(G.W.) School of Materials Science and Energy Engineering, Foshan University, Foshan 528000, China.

Author Contributions
○M.K. and Y.L. contributed equally. The manuscript was written through contributions of all authors. All authors have given approval to the final version of the manuscript.

Notes

The authors declare no competing financial interest.

■ REFERENCES

(1) Qiao, B.; Wang, A.; Yang, X.; Allard, L. F.; Jiang, Z.; Cui, Y.; Liu, J.; Li, J.; Zhang, T. Single-Atom Catalysis of CO Oxidation Using Pt_1/FeO_x. *Nat. Chem.* **2011**, 3, 634−641.

(2) Marcinkowski, M. D.; Darby, M. T.; Liu, J.; Wimble, J. M.; Lucci, F. R.; Lee, S.; Michaelides, A.; Flytzani-Stephanopoulos, M.; Stamatakis, M.; Sykes, E. C. H. Pt/Cu Single-Atom Alloys as Coke-Resistant Catalysts for Efficient C−H Activation. *Nat. Chem.* **2018**, 10, 325−332.

(3) Chen, Z.; Vorobyeva, E.; Mitchell, S.; Fako, E.; Ortuño, M. A.; López, N.; Collins, S. M.; Midgley, P. A.; Richard, S.; Vilé, G.; Pérez-Ramírez, J. A Heterogeneous Single-Atom Palladium Catalyst Surpassing Homogeneous Systems for Suzuki Coupling. *Nat. Nanotechnol.* **2018**, 13, 702−707.

(4) Shan, J.; Li, M.; Allard, L. F.; Lee, S.; Flytzani-Stephanopoulos, M. Mild Oxidation of Methane to Methanol or Acetic Acid on Supported Isolated Rhodium Catalysts. *Nature* **2017**, 551, 605−608.

(5) Flytzani-Stephanopoulos, M.; Gates, B. C. Atomically Dispersed Supported Metal Catalysts. *Annu. Rev. Chem. Biomol. Eng.* **2012**, 3, 545−574.

(6) Gates, B. C.; Flytzani-Stephanopoulos, M.; Dixon, D. A.; Katz, A. Atomically Dispersed Supported Metal Catalysts: Perspectives and Suggestions for Future Research. *Catal. Sci. Technol.* **2017**, 7, 4259−4275.

(7) Cao, K.; Zoberbier, T.; Biskupek, J.; Botos, A.; McSweeney, R. L.; Kurtoglu, A.; Stoppiello, C. T.; Markevich, A. V.; Besley, E.; Chamberlain, T. W.; Kaiser, U.; Khlobystov, A. N. Comparison of Atomic Scale Dynamics for the Middle and Late Transition Metal Nanocatalysts. *Nat. Commun.* **2018**, 9, 3382.

(8) Wang, A.; Li, J.; Zhang, T. Heterogeneous Single-Atom Catalysis. *Nat. Rev. Chem.* **2018**, 2, 65−81.

(9) Freyschlag, C. G.; Madix, R. J. Precious Metal Magic: Catalytic Wizardry. *Mater. Today* **2011**, 14, 134−142.

(10) Chen, Z. W.; Chen, L. X.; Yang, C. C.; Jiang, Q. Atomic (Single, Double, and Triple Atoms) Catalysis: Frontiers, Opportunities, and Challenges. *J. Mater. Chem. A* **2019**, 7, 3492−3515.

(11) Zhang, S.; Tang, Y.; Nguyen, L.; Zhao, Y.-F.; Wu, Z.; Goh, T.-W.; Liu, J. J.; Li, Y.; Zhu, T.; Huang, W.; Frenkel, A. I.; Li, J.; Tao, F. Catalysis on Singly Dispersed Rh Atoms Anchored on an Inert Support. *ACS Catal.* **2018**, 8, 110−121.

(12) Asakura, K.; Nagahiro, H.; Ichikuni, N.; Iwasawa, Y. Structure and Catalytic Combustion Activity of Atomically Dispersed Pt Species at MgO Surface. *Appl. Catal., A* **1999**, 188, 313−324.

(13) Fu, Q.; Saltsburg, H.; Flytzani-Stephanopoulos, M. Active Nonmetallic Au and Pt Species on Ceria-Based Water-Gas Shift Catalysts. *Science* **2003**, 301, 935−938.

(14) Zhang, X.; Shi, H.; Xu, B.-Q. Catalysis by Gold: Isolated Surface Au^{3+} Ions are Active Sites for Selective Hydrogenation of 1,3-Butadiene over Au/ZrO_2 Catalysts. *Angew. Chem., Int. Ed.* **2005**, 44, 7132−7135.

(15) Hackett, S. F. J.; Brydson, R. M.; Gass, M. H.; Harvey, I.; Newman, A. D.; Wilson, K.; Lee, A. F. High-Activity, Single-Site Mesoporous Pd/Al_2O_3 Catalysts for Selective Aerobic Oxidation of Allylic Alcohols. *Angew. Chem., Int. Ed.* **2007**, 46, 8593−8596.

(16) Lu, Y.; Wang, J.; Yu, L.; Kovarik, L.; Zhang, X.; Hoffman, A. S.; Gallo, A.; Bare, S. R.; Sokaras, D.; Kroll, T.; Dagle, V.; Xin, H.; Karim, A. M. Identification of the Active Complex for CO Oxidation over Single-Atom Ir-on-$MgAl_2O_4$ Catalysts. *Nat. Catal.* **2019**, 2, 149−156.

(17) Bruix, A.; Lykhach, Y.; Matolínová, I.; Neitzel, A.; Skála, T.; Tsud, N.; Vorokhta, M.; Stetsovych, V.; Ševčíková, K.; Mysliveček, J.; Fiala, R.; Václavů, M.; Prince, K. C.; Bruyère, S.; Potin, V.; Illas, F.; Matolín, V.; Libuda, J.; Neyman, K. M. Maximum Noble-Metal Efficiency in Catalytic Materials: Atomically Dispersed Surface Platinum. *Angew. Chem., Int. Ed.* **2014**, 53, 10525−10530.

(18) Kunwar, D.; Zhou, S.; DeLaRiva, A.; Peterson, E. J.; Xiong, H.; Pereira-Hernández, X. I.; Purdy, S. C.; ter Veen, R.; Brongersma, H. H.; Miller, J. T.; Hashiguchi, H.; Kovarik, L.; Lin, S.; Guo, H.; Wang, Y.; Datye, A. K. Stabilizing High Metal Loadings of Thermally Stable Platinum Single Atoms on an Industrial Catalyst Support. *ACS Catal.* **2019**, 9, 3978−3990.

(19) Wang, X.; van Bokhoven, J. A.; Palagin, D. Ostwald Ripening Versus Single Atom Trapping: Towards Understanding Platinum Particle Sintering. *Phys. Chem. Chem. Phys.* **2017**, 19, 30513−30519.

(20) Kwak, J. H.; Hu, J.; Mei, D.; Yi, C.-W.; Kim, D. H.; Peden, C. H. F.; Allard, L. F.; Szanyi, J. Coordinatively Unsaturated Al^{3+} Centers as Binding Sites for Active Catalyst Phases of Platinum on γ-Al_2O_3. *Science* **2009**, 325, 1670−1673.

(21) Zhang, Z.; Zhu, Y.; Asakura, H.; Zhang, B.; Zhang, J.; Zhou, M.; Han, Y.; Tanaka, T.; Wang, A.; Zhang, T.; Yan, N. Thermally Stable Single Atom Pt/m-Al_2O_3 for Selective Hydrogenation and CO Oxidation. *Nat. Commun.* **2017**, 8, 16100.

(22) Liu, J.-C.; Tang, Y.; Wang, Y.-G.; Zhang, T.; Li, J. Theoretical Understanding of the Stability of Single-Atom Catalysts. *Natl. Sci. Rev.* **2018**, 5, 638−641.

(23) Guan, H.; Lin, J.; Qiao, B.; Yang, X.; Li, L.; Miao, S.; Liu, J.; Wang, A.; Wang, X.; Zhang, T. Catalytically Active Rh Sub-Nanoclusters on TiO_2 for CO Oxidation at Cryogenic Temperatures. *Angew. Chem., Int. Ed.* **2016**, 55, 2820−2824.

(24) Liang, J.-X.; Lin, J.; Yang, X.-F.; Wang, A.-Q.; Qiao, B.-T.; Liu, J.; Zhang, T.; Li, J. Theoretical and Experimental Investigations on Single-Atom Catalysis: Ir_1/FeO_x for CO Oxidation. *J. Phys. Chem. C* **2014**, 118, 21945−21951.

(25) Qiao, B.; Liang, J.-X.; Wang, A.; Xu, C.-Q.; Li, J.; Zhang, T.; Liu, J. J. Ultrastable Single-Atom Gold Catalysts with Strong Covalent Metal-Support Interaction (CMSI). *Nano Res.* **2015**, 8, 2913−2924.

(26) Fierro-Gonzalez, J. C.; Gates, B. C. Catalysis by Gold Dispersed on Supports: The Importance of Cationic Gold. *Chem. Soc. Rev.* **2008**, 37, 2127−2134.

(27) Jones, J.; Xiong, H.; DeLaRiva, A. T.; Peterson, E. J.; Pham, H.; Challa, S. R.; Qi, G.; Oh, S.; Wiebenga, M. H.; Pereira Hernández, X. I.; Wang, Y.; Datye, A. K. Thermally Stable Single-Atom Platinum-on-Ceria Catalysts Via Atom Trapping. *Science* **2016**, 353, 150−154.

(28) Liu, J. Aberration-Corrected Scanning Transmission Electron Microscopy in Single-Atom Catalysis: Probing the Catalytically Active Centers. *Chin. J. Catal.* **2017**, 38, 1460−1472.

(29) Chupas, P. J.; Chapman, K. W.; Kurtz, C.; Hanson, J. C.; Lee, P. L.; Grey, C. P. A Versatile Sample-Environment Cell for Non-

Ambient X-ray Scattering Experiments. *J. Appl. Crystallogr.* **2008**, *41*, 822−824.

(30) Blöchl, P. E. Projector Augmented-Wave Method. *Phys. Rev. B: Condens. Matter Mater. Phys.* **1994**, *50*, 17953.

(31) Kresse, G.; Joubert, D. From Ultrasoft Pseudopotentials to the Projector Augmented-Wave Method. *Phys. Rev. B: Condens. Matter Mater. Phys.* **1999**, *59*, 1758−1775.

(32) Kresse, G.; Furthmüller, J. Efficiency of Ab-initio Total Energy Calculations for Metals and Semiconductors Using a Plane-Wave Basis Set. *Comput. Mater. Sci.* **1996**, *6*, 15−50.

(33) Perdew, J. P.; Burke, K.; Ernzerhof, M. Generalized Gradient Approximation Made Simple. *Phys. Rev. Lett.* **1996**, *77*, 3865−3868.

(34) Dudarev, S. L.; Botton, G. A.; Savrasov, S. Y.; Humphreys, C. J.; Sutton, A. P. Electron-Energy-Loss Spectra and the Structural Stability of Nickel Oxide: An LSDA+U Study. *Phys. Rev. B: Condens. Matter Mater. Phys.* **1998**, *57*, 1505−1509.

(35) Tang, Y.; Wang, Y.-G.; Li, J. Theoretical investigations of $Pt_1@CeO_2$ single-atom catalyst for CO oxidation. *J. Phys. Chem. C* **2017**, *121*, 11281−11289.

(36) Ma, D.; Li, T.; Wang, Q.; Yang, G.; He, C.; He, B.; Lu, Z.; Yang, Z. Platinum Adsorption on Ceria: A Comparative Theoretical Study of Different Surfaces. *Appl. Surf. Sci.* **2017**, *394*, 47−57.

(37) Eyring, L. The Binary Rare Earth Oxides. *Handbook on the Physics and Chemistry of Rare Earths*; Elsevier: 1979; Vol. 3, pp 337−399.

(38) Kullgren, J.; Wolf, M. J.; Mitev, P. D.; Hermansson, K.; Briels, W. J. DFT-based Monte Carlo Simulations of Impurity Clustering at CeO_2(111). *J. Phys. Chem. C* **2017**, *121*, 15127−15134.

(39) Bader, R. F. A Quantum Theory of Molecular Structure and its Applications. *Chem. Rev.* **1991**, *91*, 893−928.

(40) Li, Y.; Zakharov, D.; Zhao, S.; Tappero, R.; Jung, U.; Elsen, A.; Baumann, P.; Nuzzo, R. G.; Stach, E. A.; Frenkel, A. I. Complex Structural Dynamics of Nanocatalysts Revealed in Operando Conditions by Correlated Imaging and Spectroscopy Probes. *Nat. Commun.* **2015**, *6*, 7583.

(41) Chen, Y.; Qiu, C.; Chen, C.; Fan, X.; Xu, S.; Guo, W.; Wang, Z. Facile Synthesis of Ceria Nanospheres by $Ce(OH)CO_3$ Precursors. *Mater. Lett.* **2014**, *122*, 90−93.

(42) Jeong, D.-W.; Jang, W.-J.; Shim, J.-O.; Han, W.-B.; Kim, H.-M.; Lee, Y.-L.; Bae, J. W.; Roh, H.-S. Optimization of a Highly Active Nano-Sized Pt/CeO_2 Catalyst Via $Ce(OH)CO_3$ for the Water-Gas Shift Reaction. *Renewable Energy* **2015**, *79*, 78−84.

(43) Liu, H.-H.; Wang, Y.; Jia, A.-P.; Wang, S.-Y.; Luo, M.-F.; Lu, J.-Q. Oxygen Vacancy Promoted CO Oxidation Over Pt/CeO_2 Catalysts: A Reaction at $Pt−CeO_2$ Interface. *Appl. Surf. Sci.* **2014**, *314*, 725−734.

(44) Zhou, A.; Wang, J.; Wang, H.; Li, H.; Wang, J.; Shen, M. Effect of Active Oxygen on the Performance of Pt/CeO_2 Catalysts for CO Oxidation. *J. Rare Earths* **2018**, *36*, 257−264.

(45) Xie, P.; Pu, T.; Nie, A.; Hwang, S.; Purdy, S. C.; Yu, W.; Su, D.; Miller, J. T.; Wang, C. Nanoceria-Supported Single-Atom Platinum Catalysts for Direct Methane Conversion. *ACS Catal.* **2018**, *8*, 4044−4048.

(46) Morfin, F.; Nguyen, T.-S.; Rousset, J.-L.; Piccolo, L. Synergy Between Hydrogen and Ceria in Pt-Catalyzed CO Oxidation: An Investigation on $Pt−CeO_2$ Catalysts Synthesized by Solution Combustion. *Appl. Catal., B* **2016**, *197*, 2−13.

(47) Bera, P.; Patil, K. C.; Jayaram, V.; Subbanna, G. N.; Hegde, M. S. Ionic Dispersion of Pt and Pd on CeO_2 by Combustion Method: Effect of Metal−Ceria Interaction on Catalytic Activities for NO Reduction and CO and Hydrocarbon Oxidation. *J. Catal.* **2000**, *196*, 293−301.

(48) Bera, P.; Gayen, A.; Hegde, M. S.; Lalla, N. P.; Spadaro, L.; Frusteri, F.; Arena, F. Promoting Effect of CeO_2 in Combustion Synthesized Pt/CeO_2 Catalyst for CO Oxidation. *J. Phys. Chem. B* **2003**, *107*, 6122−6130.

(49) Pereira-Hernández, X. I.; DeLaRiva, A.; Muravev, V.; Kunwar, D.; Xiong, H.; Sudduth, B.; Engelhard, M.; Kovarik, L.; Hensen, E. J. M.; Wang, Y.; Datye, A. K. Tuning Pt-CeO2 Interactions by High-Temperature Vapor-Phase Synthesis for Improved Reducibility of Lattice Oxygen. *Nat. Commun.* **2019**, *10*, 1358.

(50) Nie, L.; Mei, D.; Xiong, H.; Peng, B.; Ren, Z.; Hernandez, X. I. P.; DeLaRiva, A.; Wang, M.; Engelhard, M. H.; Kovarik, L.; Datye, A. K.; Wang, Y. Activation of Surface Lattice Oxygen in Single-atom Pt/CeO_2 for Low-temperature CO Oxidation. *Science* **2017**, *358*, 1419−1423.

(51) DeRita, L.; Dai, S.; Lopez-Zepeda, K.; Pham, N.; Graham, G. W.; Pan, X.; Christopher, P. Catalyst Architecture for Stable Single Atom Dispersion Enables Site-Specific Spectroscopic and Reactivity Measurements of CO Adsorbed to Pt Atoms, Oxidized Pt Clusters, and Metallic Pt Clusters on TiO_2. *J. Am. Chem. Soc.* **2017**, *139*, 14150−14165.

(52) Happel, M.; Mysliveček, J.; Johánek, V.; Dvořák, F.; Stetsovych, O.; Lykhach, Y.; Matolín, V.; Libuda, J. Adsorption Sites, Metal-Support Interactions, and Oxygen Spillover Identified by Vibrational Spectroscopy of Adsorbed CO: A Model Study on Pt/Ceria Catalysts. *J. Catal.* **2012**, *289*, 118−126.

(53) Bazin, P.; Saur, O.; Lavalley, J. C.; Daturi, M.; Blanchard, G. FT-IR Study of CO Adsorption on Pt/CeO2: Characterisation and Structural Rearrangement of Small Pt Particles. *Phys. Chem. Chem. Phys.* **2005**, *7*, 187−194.

(54) Mason, M. G. Electronic Structure of Supported Small Metal Clusters. *Phys. Rev. B: Condens. Matter Mater. Phys.* **1983**, *27*, 748−762.

(55) Sun, Y.; Wang, Y.; Pan, J. S.; Wang, L.-l.; Sun, C. Q. Elucidating the 4f Binding Energy of an Isolated Pt Atom and Its Bulk Shift from the Measured Surface- and Size-Induced Pt 4f Core Level Shift. *J. Phys. Chem. C* **2009**, *113*, 14696−14701.

(56) Kowalczyk, S.; Ley, L.; Pollak, R.; Shirley, D. A. High-Resolution XPS Spectra of Ir, Pt and Au Valence Bands. *Phys. Lett. A* **1972**, *41*, 455−456.

(57) Smith, N. V.; Wertheim, G. K.; Hüfner, S.; Traum, M. M. Photoemission Spectra and Band Structures of d-Band Metals. IV. X-ray Photoemission Spectra and Densities of States in Rh, Pd, Ag, Ir, Pt, and Au. *Phys. Rev. B* **1974**, *10*, 3197−3206.

(58) Wardenga, H. F.; Klein, A. Surface Potentials of (111), (110) and (100) Oriented $CeO_{2−x}$ Thin Films. *Appl. Surf. Sci.* **2016**, *377*, 1−8.

(59) Nolan, M.; Lykhach, Y.; Tsud, N.; Skála, T.; Staudt, T.; Prince, K. C.; Matolín, V.; Libuda, J. On the Interaction of Mg with the (111) and (110) Surfaces of Ceria. *Phys. Chem. Chem. Phys.* **2012**, *14*, 1293−1301.

(60) Balaji Gopal, C.; García-Melchor, M.; Lee, S. C.; Shi, Y.; Shavorskiy, A.; Monti, M.; Guan, Z.; Sinclair, R.; Bluhm, H.; Vojvodic, A.; Chueh, W. C. Equilibrium Oxygen Storage Capacity of Ultrathin $CeO_{2-\delta}$ Depends Non-Monotonically on Large Biaxial Strain. *Nat. Commun.* **2017**, *8*, 15360.

(61) Pfau, A.; Schierbaum, K. D. The Electronic Structure of Stoichiometric and Reduced CeO2 Surfaces: An XPS, UPS and HREELS Study. *Surf. Sci.* **1994**, *321*, 71−80.

(62) Chueh, W. C.; McDaniel, A. H.; Grass, M. E.; Hao, Y.; Jabeen, N.; Liu, Z.; Haile, S. M.; McCarty, K. F.; Bluhm, H.; El Gabaly, F. Highly Enhanced Concentration and Stability of Reactive Ce^{3+} on Doped CeO_2 Surface Revealed In Operando. *Chem. Mater.* **2012**, *24*, 1876−1882.

(63) Henderson, M. A.; Perkins, C. L.; Engelhard, M. H.; Thevuthasan, S.; Peden, C. H. F. Redox Properties of Water on the Oxidized and Reduced Surfaces of CeO_2(111). *Surf. Sci.* **2003**, *526*, 1−18.

(64) Small, M. W.; Kas, J. J.; Kvashnina, K. O.; Rehr, J. J.; Nuzzo, R. G.; Tromp, M.; Frenkel, A. I. Effects of Adsorbate Coverage and Bond-Length Disorder on the d-Band Center of Carbon-Supported Pt Catalysts. *ChemPhysChem* **2014**, *15*, 1569−1572.

(65) Singh, J.; Nelson, R. C.; Vicente, B. C.; Scott, S. L.; van Bokhoven, J. A. Electronic Structure of Alumina-Supported Monometallic Pt and Bimetallic PtSn Catalysts under Hydrogen and Carbon Monoxide Environment. *Phys. Chem. Chem. Phys.* **2010**, *12*, 5668−5677.

(66) Ament, L. J. P.; van Veenendaal, M.; Devereaux, T. P.; Hill, J. P.; van den Brink, J. Resonant Inelastic X-ray Scattering Studies of Elementary Excitations. *Rev. Mod. Phys.* **2011**, *83*, 705−767.

(67) Glatzel, P.; Singh, J.; Kvashnina, K. O.; van Bokhoven, J. A. In Situ Characterization of the 5d Density of States of Pt Nanoparticles upon Adsorption of CO. *J. Am. Chem. Soc.* **2010**, *132*, 2555−2557.

(68) Jarrige, I.; Ishii, K.; Matsumura, D.; Nishihata, Y.; Yoshida, M.; Kishi, H.; Taniguchi, M.; Uenishi, M.; Tanaka, H.; Kasai, H.; Mizuki, J. i. Toward Optimizing the Performance of Self-Regenerating Pt-Based Perovskite Catalysts. *ACS Catal.* **2015**, *5*, 1112−1118.

(69) Ravel, B.; Newville, M. ATHENA, ARTEMIS, HEPHAESTUS: Data Analysis for X-ray Absorption Spectroscopy Using IFEFFIT. *J. Synchrotron Radiat.* **2005**, *12*, 537−541.

(70) Clark, A. H.; Marchbank, H. R.; Hyde, T. I.; Playford, H. Y.; Tucker, M. G.; Sankar, G. Reverse Monte Carlo Studies of CeO_2 Using Neutron and Synchrotron Radiation Techniques. *Phys. Scr.* **2017**, *92*, 034002.

(71) Zhang, F.; Jin, Q.; Chan, S.-W. Ceria Nanoparticles: Size, Size Distribution, and Shape. *J. Appl. Phys.* **2004**, *95*, 4319−4326.

(72) Migani, A.; Neyman, K. M.; Bromley, S. T. Octahedrality Versus Tetrahedrality in Stoichiometric Ceria Nanoparticles. *Chem. Commun.* **2012**, *48*, 4199−4201.

(73) Migani, A.; Vayssilov, G. N.; Bromley, S. T.; Illas, F.; Neyman, K. M. Dramatic Reduction of the Oxygen Vacancy Formation Energy in Ceria Particles: A Possible Key to Their Remarkable Reactivity at the Nanoscale. *J. Mater. Chem.* **2010**, *20*, 10535−10546.

(74) Branda, M. M.; Ferullo, R. M.; Causà, M.; Illas, F. Relative Stabilities of Low Index and Stepped CeO_2 Surfaces from Hybrid and GGA + U Implementations of Density Functional Theory. *J. Phys. Chem. C* **2011**, *115*, 3716−3721.

(75) Bruix, A.; Lykhach, Y.; Matolinova, I.; Neitzel, A.; Skala, T.; Tsud, N.; Vorokhta, M.; Stetsovych, V.; Sevcikova, K.; Myslivecek, J.; Fiala, R.; Vaclavu, M.; Prince, K. C.; Bruyere, S.; Potin, V.; Illas, F.; Matolin, V.; Libuda, J.; Neyman, K. M. Maximum Noble-Metal Efficiency in Catalytic Materials: Atomically Dispersed Surface Platinum. *Angew. Chem., Int. Ed.* **2014**, *53*, 10525−10530.